PCCP

Impedance analysis of secondary phases in Co-implanted ZnO single crystal

Journal:	*Physical Chemistry Chemical Physics*
Manuscript ID:	CP-ART-03-2014-000951.R2
Article Type:	Paper
Date Submitted by the Author:	13-May-2014

Complete List of Authors:	Younas, Muhammad; PINSTECH, Physics Division Zou, Lanlan; The University of Hong Kong, Physics Nadeem, Muhammad; PINSTECH, Physics Devision Rehman, Naeem-ur-; PIEAS, Metallurgy and Materials Engineering Su, Shi-Chen; The University of Hong Kong, Physics Zilan, Wang; The University of Hong Kong, Physics Anwand, Wolfgang; Strahlenphysik, Helmholtz-Zentrum, Wagner, A; Strahlenphysik, Helmholtz-Zentrum, Hao, Jianhua; The Hong Kong Polytechnic University , Applied Physics Leung, C.W; The Hong Kong Polytechnic University, Department of Applied Physics Lortz, Rolf; Hong Kong University of Science & Technology, Physics Li, Chi Chung; The University of Hong Kong, Physics

PCCP

RSCPublishing

Paper

Impedance analysis of secondary phases in Co-implanted ZnO single crystal

Cite this: DOI: 10.1039/x0xx00000x

M. Younas[1,2,*], Lanlan Zou[1], M. Nadeem[2], Naeem-ur-Rehman[1,3], Shi-Chen Su[1], Wang Zilan[1], W. Anwand[4], A. Wagner[4], J. H. Hao[5], C. W. Leung[5], Rolf Lortz[6], Francis C. C. Ling[1,*]

Received 00th January 2012,
Accepted 00th January 2012

DOI: 10.1039/x0xx00000x

www.rsc.org/

The Co ions of 100keV energy with a fluence of 1×10^{15} cm^{-2} are implanted into the ZnO (0001) single crystals at 300°C under vacuum. The resulting Co-implanted ZnO single crystals and the subsequent 750°C and 900°C annealed samples are analysed with respect to their structural, optical, electronic, magnetic and ac electrical properties. Photoluminescence and X-ray photoelectron spectroscopy results indicate the signatures of the Co^{2+} state and its substitution at the tetrahedrally coordinated Zn-sites. X-ray diffraction and X-ray photoelectron spectroscopy identify the presence of the $ZnCo_2O_4$, Co_3O_4 phases in the 900°C annealed sample. On comparing the resistance response of the identified phases towards different magnetic environments, the impedance spectroscopy results successfully percolate two magnetic phases ($ZnCo_2O_4$ and Co_3O_4) and a paramagnetic (Co_{Zn}) phase for 750°C and 900°C annealed samples implying the extrinsic nature of room temperature ferromagnetism. The observed ferromagnetism in each sample is not of single origin, instead mutual effects of secondary phases embedded in the paramagnetic host matrix are in competition with each other.

1. Introduction

The forecast of carrier assisted high temperature ferromagnetism in transition metal doped diluted magnetic semiconductors (especially in p-type ZnO[1]) has encouraged the scientific community to search a realistic diluted magnetic semiconductor for practical applications. The Co-ZnO material has been considered as a role model system for a wide range of diluted magnetic semiconductors after the *ab initio* theoretical prediction of intrinsic ferromagnetism[2] and the sequential experimental observation of room temperature ferromagnetism (RT FM)[3] in this class of material. Regardless of this great prospective, understanding of RT FM is still controversial whether it is intrinsic[4,5] or related to clustering or incipient development of secondary phases[6,7]or totally absent.[8,9] Furthermore, RT FM also depends upon sample preparation and growth conditions and many experimental studies have identified that RT FM is absent in near-perfect epitaxial Co-doped ZnO films.[10,11]

In order to avoid problems associated with sample preparation, ion implantation is considered to increase the sample preparation reproducibility and allow the precise control of the implanted ion concentration to overcome the solubility limit.[12] Although a substantial amount of disorder will occur after the ion implantation, ZnO exhibits a strong degree of dynamic annealing during the ion bombardment (i.e. migration, interaction and recombination of ion-beam-generated intrinsic defects). Such annealing process makes ZnO a radiation resilient material and it can bear high doses of irradiation without changing to be amorphous. However, dynamic annealing is not 100% effective for full structural recovery of the lattice disorder. Dopant clusters and extended stacking faults may also accumulate during the ion bombardment process.[13-14] Implantation at elevated temperatures may decrease the amount of disorder through the process of dynamic defect annealing and would also offer in situ thermal dopant activation[15]

Our present study aims to investigate the different possible phases and their potential role in tuning the magnetic properties of the high temperature (300°C) Co-implanted n-type ZnO single crystals. X-ray diffraction (XRD) and X-ray photoelectron spectroscopy (XPS) can reveal the crystalline and electronic structures of secondary phases respectively, but fail to offer any magnetism related information. Magnetic probes like vibrating sample magnetometers (VSM) and superconducting quantum interference devices (SQUID) can detect the overall magnetism, but are unable to distinguish between the intrinsic FM and the contribution of the multiple phases in the material under observation. Therefore, more local probe studies are needed to fairly separate the multiple phases if they are playing a role. Impedance spectroscopy (IS) is an informative and exceptional characterizing tool in fundamental and applied materials research. It can be used to resolve the contribution of the different phases to the electrical properties such as the contact effects, grains, grain boundaries, and any type of impurity inside a sample.[16,17] Compared to other techniques, IS explicitly distinguishes among the strongly coupled processes having different proceeding rates[18-20] as well as the concealed multiple phases having diverse conductivities even if the concentrations of the phases are very low.[21,22] However, conventional IS does not offer any direct magnetic information on individual phases.

In this research work, high quality single crystals have been used as the raw material to avoid the grain boundaries defects. These defects have much higher relaxation times compared to grains and normally act as a potential source to activate the RT ferromagnetism by confining transition metals or impurities.[16,23] Structural and electronic information of the phases were studied by XRD, XPS and photoluminescence (PL) and magnetic properties were investigated by VSM. IS was used to separate the potential phases and to study their magnetic properties with the measurements done without the magnetic field (NMF), with the magnetic field (MF) and then after retreating from the magnetic field (AMF). Magnetic properties of the identified phases were obtained by comparing their component resistances measured under the different magnetic environments. The origins of the observed phases were suggested according to the comprehensive information obtained from the XRD, XPS, PL and IS measurements

2. Experimental

The raw material used is the undoped melted grown ZnO (0001) single crystal obtained from the Cermet Inc., USA. Its carrier concentration and mobility are $5\times10^{16}cm^{-3}$ and $\sim203cm^2V^{-1}s^{-1}$ respectively. The Co ions of 100keV energy with a fluence of $10^{15}cm^{-2}$ were implanted into the ZnO single crystal at 300°C under vacuum. Secondary ion mass spectroscopic (SIMS) measurement carried out by the Cameca (Model IMS 4F) yielded a Co depth profile extended to a depth of 200nm and had intensity peaked at 50nm, which coincides well with the Monte Carlo TRIM calculations.[24] This corresponds to an average Co-doping concentration of $10^{19}cm^{-3}$ on the top 200nm depth. To further remove the ion-induced defects, post-implantation annealing is performed at 750°C and 900°C in Ar for 30 minutes. XRD was performed with the Bruker D8 Advance x-ray diffractometer using the Cu Kα line (0.1541nm). PL measurements were performed with the 325nm He-Cd laser line with sample mounted in a 10K closed cycled He refrigerator. The grating monochromator employed has a focal length of 500mm. The photons are detected by a photomultiplier tube (PMT) with the signal processed by a lock-in amplifier. The electronic structures of Co were studied by XPS using the MgKα line (Kratos Axis Ultra DLS system). The x-ray source and the C 1s line were taken as the standard. Magnetic measurements (M-H loop) were performed at room temperature using the Lakeshore Model 7300 series VSM. Room temperature IS measurements were performed within the frequency range of 1 Hz ≤ f ≤ 10^7 Hz using the Alpha-N analyzer (Novocontrol, Germany). To perturb the system, a low ac signal of 0.2V was used. Fully automated WINDETA software was used for interfacing the experimental setup of analyzer to the computer and for the data acquisition. The ZView (Complex Nonlinear Least Squares Immittance Data Fitting Program, Version 6.1-4/03/94) software was used for fitting and analyzing the measured impedance results within 1–2% fitting error. The IS measurements were carried out under null magnetic field (NMF), with a constant magnetic field of 0.3T perpendicular to the sample surface (MF), and 10 minutes after retreating from magnetic field (AMF).

3. Results and Discussions

3.1 Structural and electronic properties

The XRD patterns of the Co-implanted ZnO samples (Fig. 1 (a)) are dominated by the (002) peaks, which correspond to the c-axis orientated wurtzite ZnO structure. On comparison with the pure ZnO single crystals, the intensity of the (002) peaks decreases for the Co-implanted samples, indicating the implantation-induced structural changes in the samples. The two new peaks are unambiguously observed in the slow scan XRD (30.5° to 32°) of the ann900 sample as shown in Fig. 1(b). The typical (100) reflection of ZnO normally exists around 31.8° (~32°) [25,26] which is close to the newly observed peak positions in our ann900 sample. Therefore, in order to rule out the possibility of the (100) ZnO reflection due to thermally induced reconstruction of ion-induced defects, slow scan XRD for the 900°C annealed Cu-implanted ZnO single crystal prepared under the same conditions is also shown in Fig. 1(b). The lattice mismatch of Cu^{2+} ion (0.080nm) and Zn^{2+} ion (0.083nm) is very small, and may results in small lattice distortion when implanted in to ZnO.[26] Within the detection limit of XRD, no peak around 31° related to the (100) ZnO reflection is observed for the Cu-implanted ZnO single crystals annealed at 900°C (Fig. 1(b)).

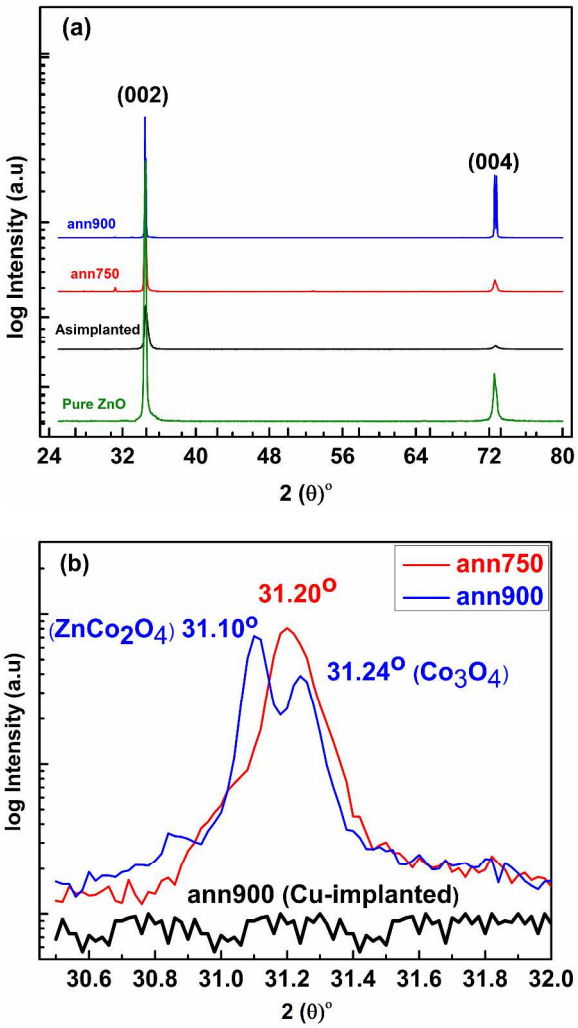

Fig. 1 (a) XRD pattern for the Co-implanted ZnO single crystal samples and (b) Slow scan XRD from 30.5° to 32° for the as-Co-implanted sample, the 750°C and 900°C annealed Cu-implanted ZnO single crystals.

Thus, the observed new peaks for the Co-implanted samples (which are below the typical (100) ZnO reflection peak around 31.8°) and the absence of the (100) ZnO reflection in the Cu-implanted ZnO single crystals suggest the presence of secondary

phases in our 900°C annealed Co-implanted samples. The two new peaks in the slow scan XRD (Fig. 1(b)) correspond to the spinel phases of $ZnCo_2O_4$ (JCPDS# 021069) and Co_3O_4 (JCPDS# 781970). Although high temperature annealing of our ann900 sample successfully show two secondary phases, we are unable to separate all the potentials phases for the ann750 sample and the broad XRD peak at 31.20° is interpreted as the superposition of the corresponding thermally induced evolving phases. These evolving phases are effectively well separated on the basis of their response towards IS (will be discussed in section 3.3). Within the detection limit of XRD, signatures related to the Co cluster and CoO are not identified. Our SIMS results (not shown here) illustrate that in the as-implanted sample, Co ions are unevenly distributed down to a depth of ~200 nm from surface with average concentration of ~ 0.60%, and this distribution profile remains unaffected even after the annealing at high temperatures (900°C).

In order to study the electronic structure of the substituted Co at the Zn site and the influence of the possible defects, PL measurements were performed at 10K for the as-Co-implanted ZnO single crystal and the post-implantation annealed samples. The dominant peak around 3.35 eV for both the un-implanted (inset of Fig. 2(a)) and the Co-implanted single crystals is related to the excitons bound to the neutral donors[27]. After annealing the Co-implanted sample at 900°C, the intensity of this band edge emission decreases, showing the introduction of annealing induced defects in this sample. PL spectra of ann750 and ann900 samples show broad green luminescence at 2.40 eV in the visible region and it increases considerably for the ann900 sample. The origin of the green luminescence is still controversial and is attributed to V_O, V_{Zn} and Cu impurity.[28,29] To take deeper insight of the annealing induced green luminescence, we compared the PL spectra of the implanted samples with the un-implanted pure ZnO single crystals (inset of Fig. 2(a)). The green luminescence was also found in both the as-grown pure ZnO single crystals and the 900°C annealed Co-implanted sample. Furthermore, our pure ZnO thin films annealed at 750°C and 900°C grown by pulsed laser deposition technique show similar green luminescence pattern (not shown here). Our observation regarding the green luminescence for single crystals and thin films suggest that the observed green luminescence is irrelevant to Co but rather an intrinsic property of single crystal and thin films. The additional peak at 1.884 eV in the implanted samples is related to the electronic transitions between the d-levels of the isolated Co^{2+} ions in a tetrahedral symmetry of oxygen atoms which shows the Co substitution at Zn site (Co_{Zn}).[30,31]

XPS has been employed to study the chemical state of Co ions in implanted samples. Fig. 2(b) shows the XPS Co 2p core level spectra. The positions and the Full Width at Half Maximum (FWHM) of peaks are presented in Table 1. For the as-implanted sample, the Co $2p_{3/2}$ peak (780.0eV) accompanied by the Co $2p_{1/2}$ peak (795.4eV) with ΔE=15.4±0.1eV indicates the existence of Co^{2+}.[32,33] Although the XPS spectra show no detectable traces of CoO and Co cluster within the detection limit of XPS, the possible existence of CoO traces cannot be ignored completely due to the existence of Co^{2+}. For ann750 sample, the positions of the $Co2p_{3/2}$, Co $2p_{1/2}$ peaks and the ΔE=15.3±0.03eV are almost the same as that of the as-implanted sample. However, the Co peak intensities of the ann750 sample is much higher, indicating more isolated character of the Co^{2+} ions. In the ann900 sample, the ΔE (=14.80±0.16 eV) is smaller than that of the as implanted and the ann750 samples. This could be due to the simultaneous existence of Co_3O_4[32] and $ZnCo_2O_4$ phases in the ann900 sample as revealed by the XRD result. The observed main Co 2p peak position in ann900 sample also has a much broader FWHM's (~9 eV), plausibly implying the co-existence of the Co^{2+} and Co^{3+} states in these Co_3O_4 and $ZnCo_2O_4$ phases. In these spinel type phases, photoelectron signals from different oxygen coordination with the Co^{2+} and Co^{3+} states are intermingled and these are normally indistinguishable by XPS.[34] Furthermore, Hays et al.[33] and Petitto et al.[35] reported that in Co_3O_4 spinel type phase, the Co^{2+} and Co^{3+} oxidation states are thermodynamically stable and inter-convertible at crystal surface, but under ambient conditions Co_3O_4 is the most stable phase.

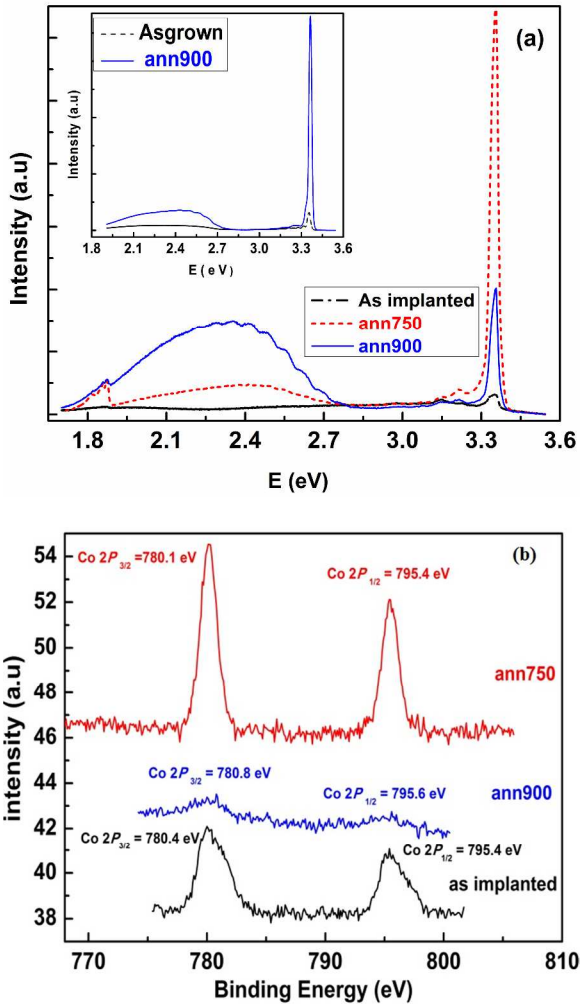

Fig. 2 (a) PL spectra for the Co-implanted samples at 10 K. Inset shows the PL spectra for the un-implanted samples, and (b) Room temperature XPS spectra of the Co *2p* peaks in the Co-implanted samples.

Table 1 Peak positions and FWHM's of the Co $2p_{3/2}$ and Co $2p_{1/2}$ peaks in the XPS spectra for the Co-implanted samples.

	Co $2p_{3/2}$ (ev)	FWHM	Co $2p_{1/2}$ (ev)	FWHM	ΔE (ev)
as-implanted	780.0±0.07	2.14	795.4±0.03	2.32	15.4±0.10
ann750	780.1±0.04	1.37	795.4±0.01	1.45	15.3±0.03
ann 900	780.8±0.15	6.68	795.6±0.17	8.67	14.8±0.16

3.2 Magnetic Properties

Room temperature M-H curve in Fig. 3 shows that the as-grown ZnO single crystal exhibits no hysteresis. For the as-implanted, ann750 and ann900 samples, FM is clearly observed in the low field region (-800G-800G). Beyond this particular field, unsaturated magnetization trends at the higher field are correlated to the paramagnetic behaviour originated from the pronounced surface spin disorder.[36] The observed magnetization is converted from emu units to μ_B/Co on the basis of the Co concentration obtained by SIMS measurement. The resultant magnetic parameters are tabulated in Table 2, indicating that the ann750 sample has lower values of remanence magnetization (Mr), saturation magnetization (Ms), and magnetic moment (μ_B/Co) compared to the ann900 sample. All the implanted samples show much smaller values of μ_B/Co (0.2-0.5μ_B/Co) than those of high-spin Co^{2+} (3μ_B/Co) and metallic Co (1.73μ_B/Co).[37] The observed weak magnetic saturation not only shows the absence of metallic Co but also intimates that the ferromagnetic magnetic signal in these samples are not mainly from the direct Co^{2+}-Co^{2+} interactions. Furthermore, it is also observed that intrinsic defects are not related to the magnetic properties of the implanted samples. Although the broad green luminescence peak in the as-grown pure ZnO single crystal (inset of Fig. 2a) indicate the existence of intrinsic defects, no FM is observed in this sample showing irrelevance of the intrinsic defects to the magnetic properties. These observations show that weak FM in these samples is not of single origin, instead different behaviours are in competition with each other. To take deeper analysis and to explore the possible origin of the weak FM, IS under magnetic field is performed on these samples.

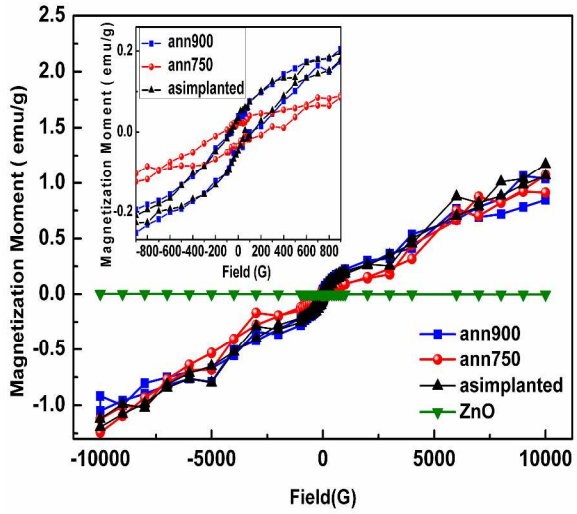

Fig. 3 Room temperature Field vs. Magnetization (M-H) graph for the Co-implanted and the pure ZnO single crystals. Inset shows the magnetization in the low field region.

Table 2 Magnetic parameters for the Co-implanted ZnO single crystal annealed at different temperatures.

	Mr (emu/g)	Ms (emu/g)	Hc (G)	μ (μ_B/Co)
as-implanted	0.05	0.19	151.16	0.478
ann750	0.02	0.09	151.16	0.213
ann 900	0.04	0.19	110.00	0.463

3.3 Impedance spectroscopy

In impedance measurements, $Z^{//}$ (the imaginary part of the impedance) vs. $Z^{/}$ (the real part of the impedance) plots generally appear in semicircular forms and the widths and heights of these semicircles are correlated with the resistive and the capacitive behaviour of the material, respectively. Different surrounding environments of the existing multiple phases and defects within the materials under observation sometime generate more than one relaxation processes. Therefore, it is a common practice during the impedance (i.e. $Z^{//}$ vs. $Z^{/}$ plots) data analysis that it is hard to spread out the competing phases when the difference in relaxation times among phases is two orders of magnitudes or less.[17,18] Different phases with approximately similar or comparable relaxation times for the involved carriers in conduction confer the more depressed semicircular arcs.

The depressed semicircular arcs normally depict smaller height than their width i.e. $Z''_{max} < ½\{Z'_{max} - Z'_{min}\}$ where Z''_{max} represents the vertical height of the semicircle, Z'_{max} and Z'_{min} represents the real axis intercepts at the lower and higher frequency sides, respectively. The difference $Z'_{max} - Z'_{min}$ (diameter of the semicircle) provides the total resistance of the sample under consideration.[17,18] Other more general observation in impedance measurement is that sometimes the semicircular arc does not pass through the origin due to other arcs having higher relaxation frequencies beyond the measurement limit.[17] In this situation we have to utilize other available formalisms for the better resolution of the competing relaxation processes.

3.3.1 Impedance plan plots ($Z^{//}$ vs. $Z^{/}$)

Room temperature IS measurements were performed on the 750°C and 900°C post-implantation annealed samples. Fig.4 shows the $Z^{//}$ against $Z^{/}$ plots of the ann750 sample taken under magnetic field. In ideal, each of the phase component would generate a semi-circular arc in the $Z^{//}$- $Z^{/}$ plot with its position dependent on the relaxation time $\tau = 1/\omega = RC$. At the maxima of the arc, the characteristic frequency is given by: $\omega_{max} = 1/RC$.[19] One large arc and a small arc with horizontal axial lengths of ~3.5 MΩ and ~900 Ω are respectively shown in Fig. 4 and its left inset.

For phases with very low resistance, only part of the corresponding arc can be seen in the $Z^{//}$- $Z^{/}$ plot if the ω_{max} is outside the available frequency range.[20] In the right inset of Fig. 4, the non-zero intercept at the low $Z^{/}$ region (i.e. the high frequency) indicates the presence of an arc with ω_{max} well above the maximum measurement frequency (i.e. 10^7 Hz). This implies that three phases are identified in the $Z^{//}$- $Z^{/}$ plot of the ann750 sample measured with the magnetic field. Similar three-phase behaviour is found in the same sample after the removal of the magnetic field.

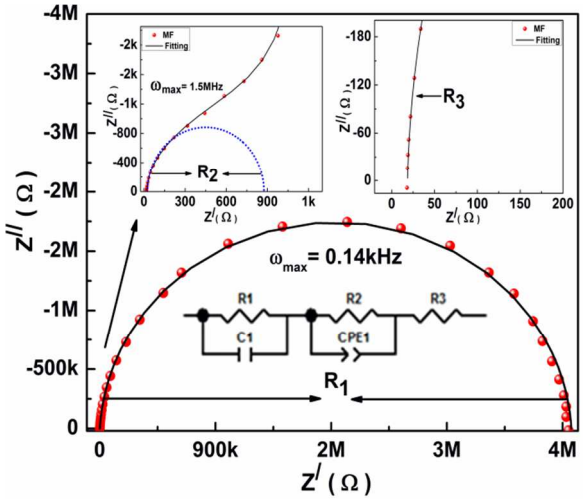

Fig. 4 Impedance plane plots for the ann750 sample under the magnetic field (MF). Frequency increases from right to left. The left and right insets are the enlarged views of the $Z^{/}$=0-1kΩ region and the $Z^{/}$=0-200Ω region, respectively. The dots, solid lines, and dashed lines represent the data, the resultant fitted lines and the contributions from the individual elements, respectively. The fitted model is also included.

In the $Z^{//}$ vs $Z^{/}$ plots of the ann750 sample measured under the null magnetic field conditions as shown in Fig. 5 and that of the ann900 sample under the different magnetic environments (not shown here), two components are visually distinguished by the distorted arc and the non-zero intercept at high frequency.

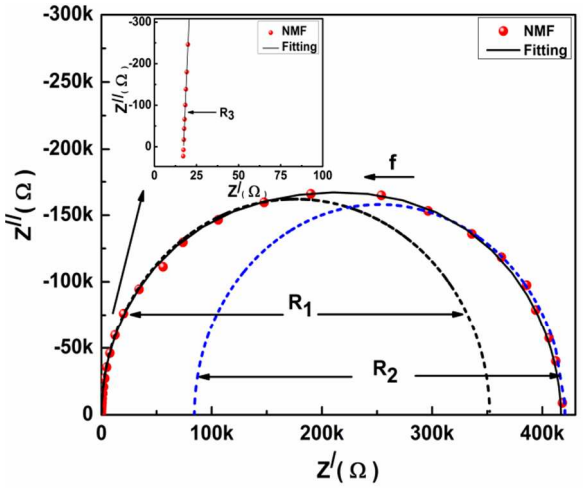

Fig. 5 Impedance plane plots for the ann750 sample under no magnetic field (NMF). Arrow shows increasing direction in frequency. The inset shows the enlarged view of the $Z^{/}$ (= 0-100Ω) region (i.e. high frequency region). The dots, solid lines, and dashed lines represent the data, resultant fitted lines and contributions from the individual elements, respectively.

Non-linear fitting was performed on all the $Z^{//}$ vs $Z^{/}$ data using the ZVIEW source code with the equivalent circuit model comprising of parallel R-CPE elements (associated with the corresponding phases) connected in series. Constant phase element CPE is given by:

$$C = (CPE)^{1/n} R^{(1-n)/n}$$

The factor *n* has limiting cases that n=1 and n=0 associated with the pure capacitive and pure resistive behaviours, respectively.[18] Based on the chi-squares obtained from the trial fitting and the heterogeneity that usually present in the post-ion-implantation annealed samples, CPE instead of capacitance is used in equivalent circuit. This is also confirmed by the large depression angles as tabulated in Table 3. The depression angles for ann750 and ann900 samples were estimated by fitting impedance plane plot using the ZVIEW software. We observe high values of the depression angle (~16°) under no magnetic field condition for single semicircle of the ann750 sample. This high depression angle indicates the presence of inhomogeneity due to the existence of the intermingled multiple phases. The value of the depression angle lowers down to ~9° for small semicircles and ~6-8° for large semicircles for the same samples in the magnetic field and the null magnetic field conditions, respectively. This indicates the improved phase stability with the application of magnetic field; this explains the observation of the three clear phases in the impedance plan plots of this sample. For the ann900 sample we observe high depression angle (~13°) indicating again the presence of diverse phases with very close relaxation times.

Table 3 The fitted parameters for the ann750 and ann900 samples of the Co-implanted ZnO single crystal in different environments. .

	ann750			ann900		
	NMF	MF	AMF	NMF	MF	AMF
R_1 (Ω)	2.31×10^5	3.71×10^6	2.21×10^5	1.53×10^5	3.24×10^3	2.41×10^3
C_1 (F)	6×10^{-10}	1×10^{-9}	10×10^{-10}	1×10^{-9}	10×10^{-10}	1.2×10^{-9}
R_2 (Ω)	1.3×10^5	980.1	2.01×10^3	4.6×10^5	621.3	8.71×10^3
CPE_2	6×10^{-10}	2.1×10^{-9}	1.9×10^{-9}	1.2×10^{-9}	8×10^{-10}	9.4×10^{-10}
n_2	0.99	0.97	0.98	0.98	0.99	0.98
C_2 (F)	7×10^{-9}	2×10^{-9}	2×10^{-9}	9.4×10^{-10}	7×10^{-10}	7×10^{-10}
R_3 (Ω)	18.28	18.13	18.93	19.65	34.47	23.61
R_t (Ω)	3.6×10^5	3.7×10^6	2.3×10^5	6.1×10^5	3.9×10^3	1.1×10^3
D.A.[a]	16.20	9.36^{C1}	9.45^{C1}	5.93	13.35	13.56
		6.18^{C2}	8.024^{C2}			

D.A.[a] is Depression Angle, C1= Small semicircle at higher frequency, C2= Large semicircle at low frequency

The $Z^{//}$- $Z^{/}$ plots were firstly fitted with the three-component model (i.e. the $(R_1CPE_1)(R_2CPE_2)(R_3CPE_3)$ model), although in some of the $Z^{//}$- $Z^{/}$ plots only two phases could clearly visually separable. Processes with relaxation times differing less than two order of magnitude cannot be clearly visually separable in the $Z^{//}$- $Z^{/}$ plot.[17,18] We have also attempted to use the two-component model on those $Z^{//}$- $Z^{/}$ plots which only showed two clearly distinguishable arcs, but we found the chi-squares were significantly inferior than those obtained by the three-component fitting. Our preliminary three-component fittings on all the samples and measuring magnetic environments have two findings, namely (1) all the fitted n_1's are effectively close to unity showing more capacitive behaviour of the associated phase, and (2) the third component is more conducting and showing metallic type behaviour. We thus dropped capacitance from the third RC component and carried out final fittings using the model of $(R_1C_1)(R_2CPE_2)(R_3)$. The best fitted results of all the parameters are tabulated in Table 3. The fitted resistance R_1, R_2 and R_3 are extracted and tabulated in Table 4 for further discussion.

Table 4 The fitted resistances R_1, R_2 and R_3 of the $Z^{//}$ vs $Z^{/}$ plots for the Co-implanted ZnO single crystals annealed at 750°C and 900°C measured in the different magnetic environments.

	R_1 (Co_3O_4)	R_2 ($ZnCo_2O_4$)	R_3 (Co_{Zn})	R_t
ann750(NMF)	2.31×10^5	1.3×10^5	18.28	3.6×10^5
MF	3.71×10^6	980.1	18.13	3.7×10^6
AMF	2.21×10^5	2.01×10^3	18.93	2.3×10^5
ann900 (NMF)	1.53×10^5	4.6×10^5	19.65	6.1×10^5
MF	3.24×10^3	621.3	34.47	3.9×10^3
AMF	2.41×10^3	8.71×10^3	23.61	1.1×10^4

It is worthy to discuss the physical origins of the three phases identified in the IS measurements. VSM and XRD data as presented previously showed that Co-cluster and pure Co^{2+} (like CoO) phases were absent in the present samples and only the $ZnCo_2O_4$ and Co_3O_4 phases are revealed by the XRD results. The Spinel type $ZnCo_2O_4$ has been reported to have high resistivity with hole/electron mediated ferromagnetic/antiferromagnetic behaviors.[38,39] The Co_3O_4 is conventionally regarded as paramagnetic with the Neil temperature T_N ~30K and has normal spinel structure.[40,41]

Regardless of the annealing temperatures and measuring magnetic environment, the R_3 is always as low as ~15-30 Ω. This is thus attributed to Co_{Zn} site because of its metallic behaviour. The possibility of Co clustering is ruled out due to the low observed magnetic moments in the magnetization data. Park et al. [42] also reported that Co clustering would occur in $Zn_{1-x}Co_xO$ with $x > 0.12$. Paramagnetic materials have magnetic dipole moment owing to incomplete cancellation of the electron spin or orbital magnetic moments. Without external magnetic field, these moments are randomly oriented and thus resulting with zero net magnetization. Under magnetic field, these magnetic dipoles are individually aligned without any mutual interaction.[43] During IS measurements in the null magnetic field and magnetic field conditions; we observe no appreciable change in R_3 in all the annealed samples. Even after retreating from the magnetic field (AMF), R_3 seems to possess its original value. The lacking response of the R_3 towards magnetic environments shows that the phase is of metallic type paramagnetic.

As shown in Table 4, the R_2's have similar magnetic behaviour for both the 750°C and 900°C annealed samples. The R_2 value under no magnetic field condition is ~10^5 Ω. It drops significantly to ~1×10^3 Ω under the magnetic field. It then slightly increases from 10^3 to 10^4 Ω after the magnetic field is removed . In antiferromagnetic materials, the spin moments of the neighbouring atoms or ions align in exactly the opposite directions. The solid as a whole thus retains no net magnetic moment.[43] Dietl et al.[44] reported that the ferromagnetic behaviour in Co-doped ZnO is due to the uncompensated spins at the surface of the antiferromagnetic Co-rich wurtzite (Zn,Co)O phase distributed in the Co-poor (Zn,Co)O paramagnetic matrix. In our case, with the applied magnetic field, the uncompensated surface spins align accordingly. This reduces the carrier scattering and thus leads to a relatively lower impedance value. When the magnetic field is removed, these uncompensated surface spins stay aligned permanently but most of the bulk spins retain its original anti-parallel orientation and reintroduce the higher value of resistance to this phase. We thus attribute this phase to the $ZnCo_2O_4$ phase.

For the 750°C annealed sample, the R_1 value under no magnetic field condition is ~10^5 Ω. Under the applied magnetic field, it increases slightly to ~10^6 Ω, and then restore back to ~10^5 Ω after the magnetic field is removed. This observation is similar to the typical superparamagnetic behaviour. One of the plausible explanations is that Ar annealing relaxes structure by freeing the adsorbed species on the phase boundary. This would render the dangling bonds to endorse the frustrated spin disorder. Under the magnetic field, frustrated surface spins randomly oriented in a spin-glass-like structure would act as a trap for charge carriers, and thus creating higher resistance.[45] After the removal of the magnetic field, this phase regains its original lower resistance. The exact origin of this superparamagnetic phase in the ann750 sample is not unambiguously known. In the ann750 samples, three component phases are competing namely the $R_1(Co_3O_4)$ with superparamagnetic behaviour, the $R_2(ZnCo_2O_4)$ phase with ferromagnetic surface and antiferromagnetic core, and finally the $R_3(Co_{Zn})$ phase having paramagnetic behaviour. The total resistance (R_t) of the ann750 sample shows the superparamagnetic type behaviour depicting appreciable influence of the superparamagnetic $R_1(Co_3O_4)$ phase to the overall ferromagnetic magnetic behaviour; therefore we observed relatively lower values of Mr, Ms, μ_B/Co and higher value of Hc for this sample as discussed previously.

For the ann900 sample, the response of the R_1 towards the magnetic field is different. The R_1 value (~10^5 Ω) under no magnetic field decreases to ~10^3 Ω when the measurements are taken under the magnetic field. It then maintains effectively the same value after the magnetic field is removed showing its ferromagnetic nature. The pure paramagnetic Co_3O_4 cannot account for this ferromagnetic behaviour, but the formation of a ferromagnetic region in the Co_3O_4 phase could offer a plausible explanation. Martin-González et al.[46] observed the surface reduction of the Co_3O_4 particle to ferromagnetic CoO in ZnO/Co_3O_4 mixture. Similar formation of CoO ferromagnetic region is likely occurred on the surface of the Co_3O_4 phase. The superparamagnetic R_1 phase observed in 750°C sample as discussed in the last paragraph could be the intermediate phase for this ferromagnetic phase formed at 900°C annealing. This is compatible with the XRD observation in which the Co_3O_4 peaks remained merged in a broad peak after 750°C annealing but it is only clearly separable after 900°C annealing (see Fig. 1 (b)). The total resistance (R_t) of ann900 sample shows ferromagnetic type behaviour depicting the appreciable influence of the ferromagnetic $R_1(Co_3O_4)$ phase to the overall magnetic behaviour of this sample.

3.3.2 Modulus ($M^{//}$ vs. log f) and loss ($Z^{//}$ vs. log f) formalisms

Up to now, we have discussed all the samples in the different environments using impedance plane plots and established the link among possible secondary phases and best fitted resistances. Impedance plane plots normally exploit the most resistive phase and the less resistive part either suppressed or may stretch out the measuring range. The electrode and interface due to space charge effects have high resistances. The high electrode resistance if present in the sample may overlap with the other high resistive phases, and can generate ambiguous result. For the successful attachment of the fitted results to the observed phases, it is therefore necessary to rule out the possibility of the electrode effects. In the following section, both the loss and modulus formalisms will be discussed simultaneously to justify the existence of the secondary phases and the exclusion of the contact effect.

Complex impedance and complex modulus are the two general electrical parameters in IS approach to differentiate the intermingled electronic process associated with substantial mixture of highly

conductive and highly resistive suspended phases. Complex impedance (Z*) and complex modulus (M*) can be calculated using the following relations of $Z^* = Z^{/} + jZ^{//}$ and $M^* = M^{/} + jM^{//} = j\omega C_o Z^*$where $Z^{/}$/$M^{/}$ and $Z^{//}$/$M^{//}$ are the real and imaginary parts of impedance and modulus, respectively, ω = 2πf, is the angular frequency, j^2 = -1 and C_o is the empty cell capacitance. For a parallel RC circuit, we have the following relations for the $Z^{/} = R/1 + (\omega RC)^2$, $Z^{//} = \omega CR^2/[1 + (\omega CR)^2]$ and $M^{/} = \omega^2 R^2 CC_o /[1 + (\omega CR)^2]$, $M^{//} = \omega RC_o/[1 + (\omega CR)^2]$.[17,18] The loss spectrum ($Z^{//}$ vs. log (f)) in impedance formalism reveals the most resistive part of the material as $Z^{//} \sim CR^2$ where R and C represents the resistance and capacitance of the associated phase. Modulus formalism ($M^{//}$ vs. log(f)) highlights the bulk properties of the material under consideration by suppressing the electrode/interfacial polarization effects due to their large capacitance as $M^{//} \sim 1/C^2R^2$. In this approach, plot of $M^{//}$ vs. log f demonstrates a maximum at a characteristic frequency in the conduction process of the relevant phase.[47- 49]

For the ann750 sample, we observed noticeable impedance behaviour as shown in Fig. 6. In the absence of magnetic field, only one distorted and asymmetric peak in both the loss and modulus spectra is observed. This broad distorted peak is correlated to the competing effects of the $ZnCo_2O_4$ and Co_3O_4 phases having comparable resistances (in consonance with the XRD result where superposition of two competing phases interpreted as a single peak). However, the application of magnetic field percolates the secondary phases by transforming the single peak into two different peaks (inset of Fig. 6). The loss spectrum shows only one peak related to the most resistive i.e. Co_3O_4 phase in this case. On the other hand, two well resolved peaks appear in the modulus formalism under the magnetic field and after the removal of the magnetic field. The lower and higher frequency peaks are coupled with the relaxation of dipoles in the low and the high conductivity Co_3O_4 and $ZnCo_2O_4$ phases, respectively. The low conductivity Co_3O_4 peaks at ~20 Hz (MF) and ~700 Hz (AMF) appear, respectively in both the $M^{//}$ vs log f and $Z^{//}$ vs log f plots (inset of Fig. 6.) implying that there are no electrode and interfacial effects. It is because of the fact that the electrode/interfacial effects if present would appear as the most dominant peak in the loss spectrum ($Z^{//}$ vs. log f) due to their high resistance.

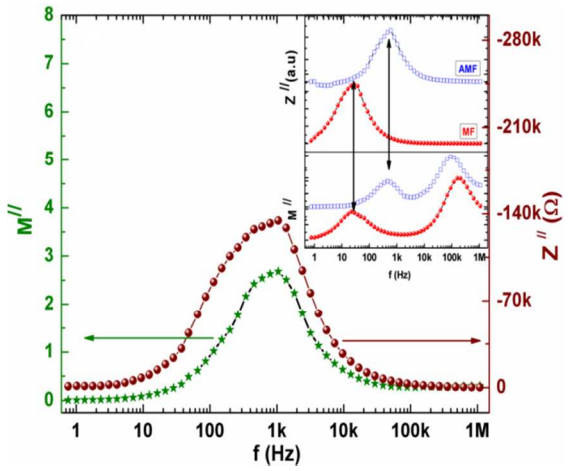

Fig. 6 The $M^{//}$ vs. log (f) and $Z^{//}$ vs log (f) plots for the ann750 sample measured in the null magnetic field condition (NMF). The inserts show the $M^{//}$ vs. log (f) and $Z^{//}$ vs log (f) plots measured within the magnetic field (MF) and after the removal from the magnetic field (AMF) for the same sample.

On comparing these findings with the previous studies carried out by Wikberg et. al[50] and Ney et al. [51] on Co-implanted ZnO single crystals, we successfully percolated two spinel type secondary phases imbedded in the ZnO host matrix by combining impedance results with the other spectroscopic techniques. In both these studies, the Co ions (100 keV energy) were implanted into ZnO single crystals at room temperature with higher flux values and lower annealing temperatures compared to our case. No spinel type secondary phase was observed in their XRD spectra of the as-implanted and annealed samples, instead a Co_2Zn alloy was observed.[50] However it was argued that for the consistent explanation of the observed ferromagnetic behaviour at least one ferromagnetic (ferrimagnetic) component with transition temperature more close to room temperature is still required.[50] One of the possible reasons for their complete failure in filtering out all the potential phases inside the sample is related to the low annealing temperatures of 800ºC[50] and 450ºC.[51] At these low annealing temperatures, thermally induced phases may superimposed and remains undetected by XRD similar to our case for the ann750 sample, but these phases were effectively well separated by IS. The other possibility is the utilization of the high implantation dose in the above-discussed studies. At comparatively low defect concentrations, the efficiency of the ZnO surface on dynamic annealing may be higher leading to the more relaxed surface. The free ZnO surface acting as a defect sink at low fluence (similar to our case with fluence ~ 1×10^{15}cm^{-2}) provides support to the dopant ions to find enough time and energy to settle down to form the spinel type secondary phases. On the other hand, at higher fluence, the defect sink properties of the surface might be degraded or dominated by the high defect concentration, leading to a more uniformly damaged surface.[15,52] The damaged surface with higher fluence (~ 5×10^{16} cm^{-2} in the above discussed study[50]) might provide high energy to the dopant ions to form Co_2Zn alloy along with the formation of other small size secondary phases that remained unnoticed by XRD due to the detection limit problem.

4. Conclusions

We have studied the secondary phases in Co-implanted ZnO using a comprehensive spectroscopic approach. PL and XPS results indicate the signature of the Co^{2+} state and its substitution at tetrahedrally coordinated Zn-site. XRD patterns for the ann900 sample reveals the $ZnCo_2O_4$ and Co_3O_4 phases after the heat treatment. The impedance data are fitted with the three components model $(R_1C_1)(R_2CPE_2)(R_3)$ within the null magnetic field , under magnetic field and after the removal of the magnetic field environments for the ann750 and ann900 samples. IS results successfully differentiated the magnetic $ZnCo_2O_4$ and Co_3O_4 secondary phases in the Co-implanted ZnO as well as the paramagnetic Co_{Zn} phase. The coincidences of the observed relaxation frequencies of both the loss and modulus spectra eliminate the electrode interferences and show the real picture of the material. The observed FM in each sample is not of single origin but instead it is the joint effects of the secondary phases embedded in the paramagnetic host matrix. We suggest that the secondary phases are present all the time in the annealed samples but their thermal stability and mix relaxation frequencies limits the resolution. Although, the Co concentration is low in our samples, we have shown that impedance spectroscopy measurement under magnetic field is a powerful tool to deliberately percolate the intermingled phases when they are present with different conductivities.

Acknowledgements
The work presented here was supported by the RGC, HKSAR under the GRF (HKU703612P) and SEG_HKUST03, as well as HKU Seed Funding Program for Basic Research (201111159037), and the National Natural Science Foundation of China (No.61205037). We are also thankful to the EMMG, PINSTECH, Nilore, Islamabad, Pakistan for providing the IS facilities.

Notes and references

1Department of Physics, The University of Hong Kong, Pokfulam Road, Hong Kong, P. R. China
2EMMG, Physics Division, PINSTECH, P.O. Nilore, Islamabad, Pakistan.
3Department of Metallurgy and Materials Engineering, PIEAS, Nilore, Islamabad 45650, Pakistan.
4Institute für Strahlenphysik, Helmholtz-Zentrum Dresden-Rossendorf, Postfach 510119, D-01314 Dresden, Germany.
5Department of Applied Physics, The Hong Kong Polytechnic University, Hong Kong, P. R. China.
6Department of Physics, Hong Kong University of Science and Technology, Clear Water Bay, Hong Kong, P. R. China
*chuhan.pieas@gmail.com (M. Younas)
*ccling@hku.hk (C. C. Ling)

1 T. Dietl, H. Ohno, F. Matsukura, J. Cibert, and D. Ferrand, *Science,* 2000, **287,** 1019.
2 K. Sato, and H. Katayama-Yoshida, *Jpn. J. Appl. Phys.,* 2000, **39**, L555.
3 K. Ueda, H. Tabata, and T. Kawai, *Appl. Phys. Lett.,* 2001, **79**, 988.
4 C. D. Pemmaraju, R. Hanafin, T. Archer, H. B. Braun, and S. Sanvito, *Phys. Rev. B,* 2008, **78**, 054428.
5 G. Ciatto, A. Di Trolio, E. Fonda, P. Alippi, A. M. Testa, and A. A. Bonapasta, *Phys. Rev. Lett.*, 2011, **107**, 127206.
6 S. Yin, M. X. Xu, L. Yang, J. F. Liu, H. Rösner, H. Hahn, H. Gleiter, D. Schild, S. Doyle, T. Liu, T. D.. Hu, E. Takayama-Muromachi, and J. Z. Jiang, *Phys. Rev. B,* 2006, **73**, 224408.
7 T. C. Kaspar, T. Droubay, S. M. Heald, M. H. Engelhard, P. Nachimuthu, and S. A. Chamber, *Phys. Rev. B,* 2008, **77**, 201303(R).
8 C. N. R. Rao and F. L. Deepak, *J. Mater. Chem.*, 2005, **15**, 573.
9 Z. Jin, T. Fukumura, M. Kawasaki, K. Ando, H. Saito, T. Sekiguchi, Y. Z. Yoo, M. Murakami, Y. Matsumoto, T. Hasegawa, and H. Koinuma, *Appl. Phys. Lett.,*2001, **78**, 3824.
10 A. Ney, T. Kammermeier, K. Ollefs, S. Ye, V. Ney, T. C. Kaspar, S. A. Chambers, F. Wilhelm, and A. Rogalev, *Phys. Rev. B*, 2010, **81**, 054420.
11 A. Ney, M. Opel, T. C. Kaspar, V. Ney, S. Ye, K. Ollefs, T. Kammermeier, S. Bauer, K. W. Nielsen, S. T. B. Goennenwein, M. H. Engelhard, S. Zhou, K. Potzger, J. Simon, W. Mader, S. M. Heald, J. C. Cezar, F. Wilhelm, A. Rogalev, R. Gross, and S. A. Chambers, *New J. Phys.,* 2010, **12**, 013020.
12 S. Zhou, K. Potzger, G. Talut, H. Reuther, J. von Borany, R. Gro¨tzschel, W. Skorupa, M. Helm, J. Fassbender, N. Volbers, M. Lorenz, and T. Herrmannsdorfer, *J. Appl. Phys.,* 2008, **103**, 023902.
13 S. O. Kucheyev, J. S. Williams, C. Jagadish, J. Zou, C. Evans, A. J. Nelson, and A. V. Hamza, *Phys. Rev. B*, 2003, **67**, 094115.
14 A. Yu. Azarov, A. Hallén, X. L. Du, P. Rauwel, A. Yu. Kuznetsov, and B. G. Svensson, *J. Appl. Phys*. 2014, **115**, 073512.
15 M. A. Myers, M. T. Myers, M. J. Genera, J. H. Lee, L. Shao, and H. Wang, *Appl. Phys. Lett.* 2012, **101**, 112101.
16 J. C. A. Huang and H. S. Hsu, *Appl. Phys. Lett.,* 2005, **87**, 132503.
17 J. R. Macdonald, *Impedance Spectroscopy Emphasing Solid Materials and Systems,* Wiley, New York, 1987.
18 E. Barsoukov, J. R. Macdonald, *Impedance Spectroscopy Theory, Experiments and Applications,*John Wiley, New Jersey, 2nd edn., 2005.
19 D. C. Sinclair and A. R. West, *J. Appl. Phys.,* 1989, **66**, 3850.
20 D. C. Sinclair, T. B. Adams, F. D. Morrison, and A. R. West, *Appl. Phys. Lett.,* 2002, **80**, 2153.
21 P.B. Macedo, C.T. Maynihan, and R. Bose, *Phys. Chem. Glasses,* 1972, **13,** 171.
22 V. Rovenzano, L.P. Boesch, V. Volterra, C.T. Moynihan, and P.B. Macedo, *J. Am. Cream. Soc.*, 1972, **55,** 492.
23 H. S. Hsu, J. C. A. Huang, S. F. Chen, and C. P. Liu, *Appl. Phys. Lett.,* 2007, **90**, 102506.
24 J. F. Ziegler, J. P. Biersack, and U. Littmark, *The Stopping and Range of Ions in Solids,* Pergamon, New York, 1985.
25 X. Penga, J. Xub, H. Zanga, B. Wangb, Z. Wang, *J. Lumin.,* 2008, ***128***, 297.
26 G. K. Mani, J. B. B. Rayappan, *J. Alloys Compd.,* 2014, **582,** 414.
27 P. A. Rodnyi and I. V. Khodyuk, *Opt. Spectrosc.,* 2011, **111,** 776.
28 E. Biegger, M. Fonin, U. Rüdiger, N. Janßen, M. Beyer, T. Thomay, R. Bratschitsch and Yu. S. Dedkov, *J. Appl. Phys.,* 2007, **101**, 073904.
29 H. S. Kang, J. S. Kang, J. W. Kim, and S. Y. Lee, *J. Appl. Phys.,* 2004, **95**, 1246.
30 V. V. Strelchuk, V. P. Bryksa, K. A. Avramenko, P. M. Lytvyn, M. Ya. Valakh, V. O. Pashchenko, O. M. Bludov, C. Deparis, C. Morhain, and P. Tronc, *Semicond. Phys. Quantum Electron. Optoelectron.,* 2011, **14,** 31.
31 J. W. Quilty, A. Shibata, J.Y. Son, K. Takubo, T. Mizokawa, H. Toyosaki, T. Fukumura, and M. Kawasaki, *Phys. Rev. Lett.,* 2006, **96,** 027202.
32 J. F. Moulder, W. F. Stickle, P. E. Sobol, K. D. Bomben, *Handbook of X-ray Photoelectron Spectroscopy,*Perkin–Elmer, Eden Prairie, 1992.
33 J. Hays, K. M. Reddy, N. Y. Graces, M. H. Engelhard, V. Shutthanandan, M. Lue, C Xu, N. C. Giles, C. Wang, S. Thevuthasan, and A. Punnoose, *J. Phys.: Condens. Matter,* 2007, **19,** 266203.
34 B. J. Tan, K. J. Klabunde, and Peter M. A. Sherwood, *J. Am. Chem. Soc.*, 1991**, 113**, 855 (1991).
35 S. C. Petitto, E. M. Marsh, G. A. Carson, and M. A. Langell, *J. Mol. Catal. A: Chem.,* 2008, **281**, 49.
36 M. Younas, M. Nadeem, M. Atif, and R. Grossinger, *J. Appl. Phys.,2011,* **109**, 093704.
37 M. Ivill, S. J. Pearton, S. Rawal, L. Leu, P Sadik, R Das, A. F. Hebard, M. Chisholm, J. D. Budai, and D. P . Norton, *New J. Phys.,* 2008, **10,** 065002.
38 M. Dekkers, G. Rijnders, and Dave H. A. Blankb, *Appl. Phys. Lett,* 2007*,* **90**, 021903.
39 H. J. Kim, I. C. Song, J. H. Sim, H. Kim, D. Kim, Y. E. Ihm, and W. K. Choo, *J. Appl. Phys.,* 2004, **95**, 7387.
40 P. Dutta, M. S. Seehra, S. Thota, and J Kumar, *J. Phys. Condens. Matter, 2008,* **20,** 015218.
41 M. Hamdani, R.N. Singh, and P. Chartier, *Int. J. Electrochem. Sci.*, 2010, **5,** 556.
42 J. H. Park, M. G. Kim, H. M. Jang, S. Ryu1, and Y. M. Kim, *Appl. Phys. Lett.,* 2004, **84**, 1338.
43 B. D. Cullity, *Introduction to Magnetic Materials*, Addison-Wesley, Readings, Massachusetts, *2nd edn.,* 1978.

44 T. Dietl, T. Andrearczyk, A. Lipińska, M. Kiecana, Maureen Tay, and Yihong Wu, *Phys. Rev. B,* 2007, **76**, 155312.
45 M. Younas, M. Atif, M. Nadeem, M. Siddique, M. Idrees, and R. Grossinger, *J. Phys. D: Appl. Phys.,* 2011 **44** 345402.
46 M. S. Martin-Gonzalez, J. F. Fernandez, F. Rubio-Marcos , I. Lorite, J. L. Costa-Kramer, A. Quesada, M. A. Banares, and J. L.G. Fierro, *J. Appl. Phys.*, 2008, **103**, 083905.
47 P. B. Macedo, C. T. Maynihan, and R. Bose, *Phys. Chem. Glasses,* 1972, **13,** 171.
48 V. Rovenzano, L. P. Boesch, V. Volterra, C. T. Moynihan, and P. B. Macedo, *J. Am. Cream. Soc.,*1972**, 55,** 492.
49 I. M. Hodge, K. L. Ngai, and C. T. Moynihan, *J. Non-Cryst. Solids,* 2005, **351,** 104.
50 J. M. Wikberg, R. Knut, A. Audren, M. Ottosson, M. K. Linnarsson, O. Karis, A. Hallén, and P. Svedlindh, *J. Appl, Phys.,*2011, **109**, 083918.
51 V. Ney, S. Ye, T. Kammermeier, A. Ney, H. Zhou, J. Fallert, H. Kalt, F. Y. Lo, A. Melnikov, and A. D. Wieck, *J. Appl, Phys.,*2008, **104**, 083904.
52 M. T. Myers, S. Charnvanichborikarn, L. Shao, and S. O. Kucheyev, *Scr. Mater*., 2012, **67**, 65